

J_0 is the zero-order Bessel function, and γ_{0n} is the n th zero of its first derivative. In the asymmetric case, the force involves a sum of an attractive domain correlation and a repulsive double-layer forces.

Equations 5 and 7 provide a qualitative explanation of the following observations: (i) adding electrolyte (that is, increasing κ) weakens the force; (ii) if $\sigma(r, \theta)$ scales with the domain size, then the force is independent of R_D for $R_D \gg D$, $R_D \gg \kappa^{-1}$, or both; (iii) as the domain size decreases with increasing temperature, a transition occurs from a regime where the force is insensitive to changes in R_D to a regime where the force decreases sharply with decreasing R_D ; (iv) the magnitude of the force is consistent with reasonable values of σ ; that is, $\sigma_{max} \approx 0.01 \text{ C/m}^2$ is more than enough to yield the observed long-range forces; (v) attractive forces in the symmetric and asymmetric systems arise from the same basic mechanism; and (vi) if, in the asymmetric case, the attractive component wins over the repulsive at some separation, it does so at all separations.

However, Eqs. 5 and 7 do not explain the data quantitatively. In particular, (i) contrary to observations, the force is predicted to be weaker in the symmetric case than in the asymmetric case and (ii) the predicted dependence on κ is too weak to quantitatively account for the observations. In our view, lack of agreement is partly caused by the approximation imposed by linearization of the PB equation. (iii) Finally, the above theory in combination with the van der Waals theory does not account for the strongly attractive component of the force that appears at the shorter range and has an apparent decay constant in the range 1.5 to 3.5 nm. This short-ranged interaction may directly measure the hydrophobic attraction; however, it could equally well arise by domain correlation combined with a rearrangement of domain sizes caused by the interaction between the surfaces as they move together.

REFERENCES AND NOTES

1. J. N. Israelachvili and R. M. Pashley, *Nature* **300**, 341 (1982).
2. R. M. Pashley, P. M. McGuiggan, B. W. Ninham, D. F. Evans, *Science* **229**, 1088 (1985).
3. H. K. Christenson, J. Fang, B. W. Ninham, J. L. Parker, *J. Phys. Chem.* **94**, 8004 (1990); and references therein.
4. K. Kurihara, S. Kato, T. Kunitake, *Chem. Lett.* **9**, 1553 (1990).
5. Y.-H. Tsao, S. X. Yang, D. F. Evans, H. Wennerström, *Langmuir* **7**, 3154 (1991).
6. F. Podgornik, *J. Chem. Phys.* **91**, 5840 (1989).
7. P. J. Attard, *J. Phys. Chem.* **93**, 6441 (1989).
8. Y. Okahata, R. Ando, T. Kunitake, *Bunsenges. Physik. Chem. Ber.* **85**, 789 (1981).
9. The chain melting temperatures of dialkyldimethylammonium surfactants in ethylene glycol were

measured with a Perkin-Elmer DSC 7 differential scanning calorimeter.

10. Y.-H. Tsao, D. F. Evans, H. Wennerström, *Langmuir* **9**, 779 (1993).
11. P. J. Scales, F. Grieser, T. W. Healy, *Thin Solid Films* **215**, 223 (1992).
12. For further discussion, see (10).
13. G. Binnig, C. F. Quate, Ch. Gerber, *Phys. Rev. Lett.* **56**, 930 (1988).
14. L. Bergstrom and R. J. Pugh, *J. Am. Ceram. Soc.* **72**, 103 (1989); L. Bergstrom and E. Bostedi, *J. Colloid Interface Sci.* **49**, 183 (1990).
15. N. A. Burnham and R. J. Colton, in *Scanning Tunneling Microscopy: Theory and Applications*, D. Bonnell, Ed. (VCH, New York, 1992), chap. 2; G. Lee, thesis, University of Minnesota (1992).
16. One of the V-shaped cantilevers on a monolayer-coated AFM cantilever substrate (Digital Instruments) was removed and glued onto a stainless steel disk with the Si_3N_4 -monolayer side up. An optical microscope was used to locate the monolayer-coated cantilever for the AFM imaging.
17. B. V. Derjaguin, *Kolloid Z.* **69**, 155 (1934).
18. J. L. Parker and P. M. Claesson, *Langmuir* **8**, 757 (1992).
19. H. M. McConnell, L. K. Tamm, R. M. Weis, *Proc. Natl. Acad. Sci. U.S.A.* **81**, 3249 (1984); H. Möhwald, *Annu. Rev. Phys. Chem.* **41**, 411 (1990).
20. This work was supported by the National Institutes of Health (GM34341).

19 April 1993; accepted 1 September 1993

A Direct Measurement of the Terrestrial Mass Accretion Rate of Cosmic Dust

S. G. Love and D. E. Brownlee

The mass of extraterrestrial material accreted by the Earth as submillimeter particles has not previously been measured with a single direct and precise technique that samples the particle sizes representing most of that mass. The flux of meteoroids in the mass range 10^{-9} to 10^{-4} grams has now been determined from an examination of hypervelocity impact craters on the space-facing end of the Long Duration Exposure Facility satellite. The meteoroid mass distribution peaks near 1.5×10^{-5} grams (200 micrometers in diameter), and the small particle mass accretion rate is $(40 \pm 20) \times 10^6$ kilograms per year, higher than previous estimates but in good agreement with total terrestrial mass accretion rates found by geochemical methods. This mass input is comparable with or greater than the average contribution from extraterrestrial bodies in the 1-centimeter to 10-kilometer size range.

The Earth's meteoritic mass accretion rate plays an important role in many contexts. It constrains models of the interplanetary meteoroid population and of the zodiacal light (1), facilitates assessment of the importance of exogenous materials both on other planets (2, 3) and in the development of life on Earth (4–6), provides calibration for the use of Os isotopes and Ir abundances as tracers for estimation of terrestrial sedimentation and large impact rates (7–9), imposes constraints on the influence of extraterrestrial ^3He in the isotopic composition of terrestrial materials (10), and quantifies meteoroid collision hazards for spacecraft. The Earth's accretion rate of meteoritic material in a single typical year is believed to be dominated by submillimeter particles (4, 5, 9, 11), as evidenced by spacecraft meteoroid detectors and optical and radar meteor studies, whereas the average contribution from 1000-ton and larger bodies may dominate the flux on longer time scales (12–14). Unfortunately, the implied peak of the micrometeoroid mass distribution occurs at particle sizes between 0.1 and 1.0 mm, where the flux is below the detection limit of previous spacecraft studies and the mete-

oroid kinetic energy is inadequate for mass determination by optical meteor techniques (1, 11, 15). Radar meteor studies sample this size range, but uncertainties in the extraction of meteoroid masses from radar echo data lead to a two orders of magnitude mismatch with the spacecraft-derived mass flux at the radar detection limit of $\sim 10^{-6}$ g, leading to an at least half an order of magnitude uncertainty in the integrated micrometeoroid mass accretion rate derived by this method (11).

We have determined the mass flux and size distribution of micrometeoroids in the critical submillimeter size range by measuring hypervelocity impact craters found on the space-facing end of the gravity-gradient-stabilized Long Duration Exposure Facility (LDEF) satellite. A number of factors establish the unprecedented reliability of this approach: the large area and exposure time of the collection surfaces, their constant (always within 1°) zenith-pointing attitude, and a wealth of empirical data that allow projectile energies to be accurately determined from the sizes of craters in solid aluminum targets.

A set of 761 craters was found on 5.6 m² of "thermal control panel" surfaces exposed to space for 5.77 years at altitudes ranging from 480 to 331 km. The panels were

Department of Astronomy, FM-20, University of Washington, Seattle, WA 98195.

formed from 1.6-mm-thick sheets of 6061-T6 aluminum alloy. Their orientation was ideal for measurement of the meteoroid flux. The rigid directional control of LDEF eliminated shielding by the Earth and minimized the effects of ram-direction flux enhancement. The flat exposure geometry excluded the possibility of shielding by other parts of the satellite, as well as spurious craters caused by high-speed ejecta from impacts elsewhere on the spacecraft. The zenith-facing attitude also greatly reduced the flux of anthropogenic orbital debris, which is most evident on surfaces facing the spacecraft's apex direction. The ratio of measured crater surface densities on the Earth-facing and space-facing ends (16), combined with the requirement that the flux of particles on bound orbits at the two surfaces be identical and allowing for a possible underrepresentation of bound particle impacts on the Earth-facing end (which was tipped 1° away from the ram direction), suggests that fewer than 10% of the space end craters in the 100- μm to 1-mm size range were produced by orbital debris, a negligible contribution in view of the other uncertainties involved. Finally, the satellite's orbital inclination of 28°, combined with the Earth's axial tilt of 23.5° and the multiyear mission duration, ensures that its space-facing end sampled a wide variety of directions with respect to the apex of the Earth's orbital motion. The craters on those surfaces therefore provide a faithful, directionally averaged record of the terrestrial micrometeoroid flux. Typical craters are simple hemispherical cavities with easily determined dimensions.

Three different sets of craters were used in this study. The first was obtained by a naked-eye scan of thermal control panels H16 and H22 (total area 1.2 m²), complete down to 100 μm crater diameter and comprising 552 craters. The second set (97 craters) was acquired in a microscope scan of 0.0521 m² and was complete to 20 μm diameter, the limit below which imperfections in the anodized panel surfaces made identification of impact features unreliable. A third set of craters was obtained by combining a visual scan of 57 features larger than 0.5 mm on all 3.4 m² of the 10 panels (H14 through H18 and H20 through H24) available for analysis by us, plus spatially calibrated digital images of 55 additional large craters on the unavailable panels H13, H19, and H25. The latter sample represents 2.2 m² and is an important addition to the large crater population.

We measured the diameters and the depths of all 609 visual impact craters used in this study. Diameters alone were measured for the craters found in the microscope scan. Diameter measurements were obtained by imaging each crater with a

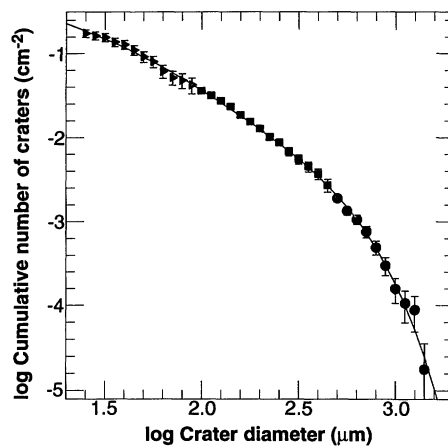


Fig. 1. Cumulative crater density as a function of diameter. Squares, craters found by the optical scan, complete down to 100 μm diameter; circles, combination of data from a larger optical scan and digital imagery of craters on additional panels not available for direct study by us; and triangles, craters in the microscope scan. A polynomial fit to the data, included here for comparison to other crater density measurements and to simplify reinterpretation in the case of future improvements to the projectile penetration formula, is of the form $\log n = 8.8749 - 25.439 \log d + 28.054 (\log d)^2 - 15.536 (\log d)^3 + 4.1732 (\log d)^4 - 0.44175 (\log d)^5$

Zeiss GFL compound microscope mounted on a large, manually driven xy traveling stage. Vertical focusing was accomplished with a motor drive, and vertical position measured with a digital micrometer to an accuracy of 1.5 μm . The images were obtained with a $\sim 3\text{-}\mu\text{m}$ depth of focus objective focused at the "datum" plane of the aluminum surrounding each crater and were recorded with a charge-coupled device (CCD) camera coupled to a video printer. The intersection of the crater bowl with the datum plane was seen as a thin ring in sharp focus. The diameter of each crater ring was measured from the video printer images to an accuracy of a few percent. The diameters of eccentric craters were taken as the means of their major and minor axes.

The 55 large craters on panels H13, H19, and H25 were imaged by See *et al.* (17) with a Wildt stereo microscope at Kennedy Space Center (KSC) before the panels were removed from the spacecraft. The image archive included frames of distance calibration standards, which we used to find the crater diameters. Although the depth of field of the digital images is large, we "calibrated" them by comparing measurements of craters obtained with both systems. We believe that any systematic error in diameter measurements between the two microscopes is less than 10%.

Depths were measured by recording the change in focus distance between the datum plane and the crater bottom with use of the narrow depth of focus objective, which was accurate to within $\pm 3 \mu\text{m}$ (for a typical depth of $\sim 50 \mu\text{m}$). Depth measurements were unavailable for the small crater set and for the KSC craters. The crater diameter measurements lead to a cumulative size-frequency distribution (Fig. 1). Correcting for exposure geometry effects, the crater density curve is consistent with results from the Solar Maximum Mission satellite (18) and other LDEF surfaces (19).

The space end crater measurements illustrated in Fig. 1 provide reliable informa-

tion about the meteoroids that created them and are the basis for determination of the projectile mass spectrum. Cratering in soft metals, unlike most other meteoroid detection methods, is not seriously plagued by spurious detections, calibration uncertainties, or limited dynamic range. Empirical relations can be used to extract a distribution of projectile masses from crater measurements if the impactor velocity and target properties are known (20–22).

Unfortunately, the most well-developed relations between crater dimension and projectile properties utilize crater depth, not diameter (20, 21); this would restrict our sample to the range of crater sizes where accurate depth information is available. It is possible, however, to relate crater depths and diameters, given their simple geometries (Fig. 2). The mean depth-diameter ratio is 0.527. There is no significant systematic variation in that value with crater size (17).

Using the polynomial fit to the crater size-frequency distribution along with the mean depth-diameter ratio, we calculated a meteoroid mass distribution with an empirically determined formula for hypervelocity impacts in thick aluminum alloy targets (21)

$$P = 5.24d^{1.056}H^{-0.25} \left(\frac{\rho_p}{\rho_t}\right)^{0.5} \left(\frac{v_n}{c}\right)^{0.667} \quad (1)$$

where P and d are the penetration depth and projectile diameter, respectively, in centimeters; H is the Brinnell hardness of the target; ρ_p and ρ_t are the projectile and target densities in grams per cubic centimeter; and v_n and c are the component of projectile velocity normal to the target surface and the sound speed in the target material, both in kilometers per second. Crater volume is roughly proportional to the impactor kinetic energy. For 6061-T6 aluminum, $H = 90$, $\rho_t = 2.7 \text{ g cm}^{-3}$, and $c = 6.1 \text{ km s}^{-1}$ (23). We chose ρ_p to be 2.5 g cm^{-3} , consistent with previous studies

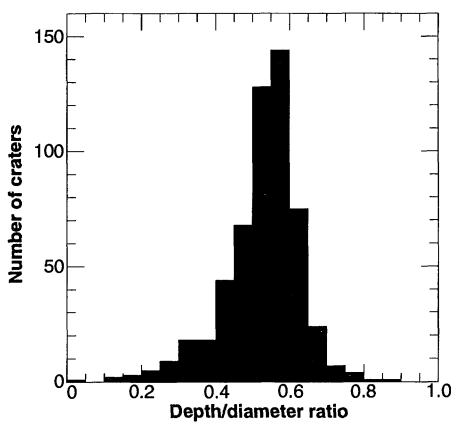


Fig. 2. Depth-diameter ratio distribution of visual scan craters. The average value of 0.527 was used to convert the diameter distribution of Fig. 1 into depths, which were used to find projectile energies.

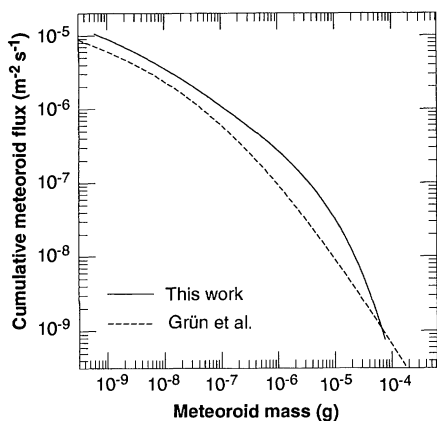


Fig. 3. Cumulative micrometeoroid flux onto the Earth. The depicted curve is computed from the polynomial fit of Fig. 1. The model of Grün *et al.* (7) is shown for comparison, after removal of the gravitational defocusing adjustment applied by them to convert their near-Earth flux to an interplanetary one.

and our own measurements of the densities of stratospheric cosmic dust particles (1, 18, 24). We chose the average meteoroid speed to be 16.9 km s^{-1} , as found by Erickson (25) and Kessler (26) for photographic meteors and supported by crater rate measurements on LDEF (27, 28); this value corresponds to a v_n of 12.0 km s^{-1} , assuming an average flight angle of 45° with respect to the local zenith. The satellite's 8 km s^{-1} velocity vector lies in the target surface plane and hence does not affect the normal component of the impact velocity.

The major source of uncertainty in this treatment, and especially in the mass accretion rate discussed below, lies in the value of the encounter velocity. Detailed knowledge of the micrometeoroid velocity and flight angle distributions may allow this calculation to be improved in the future. A

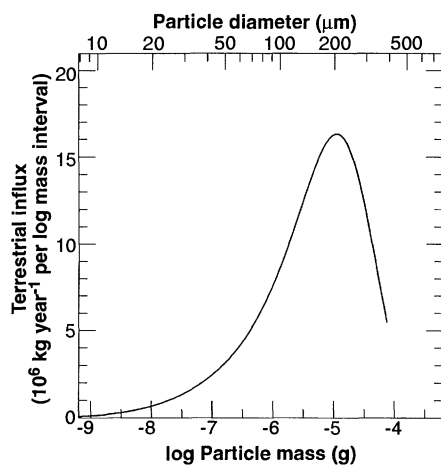


Fig. 4. Mass of micrometeorites accreted by the Earth annually per log differential particle mass interval. Note the strong peak near $1.5 \times 10^{-5} \text{ g}$ showing that most of the mass incident upon the Earth as micrometeoroids occurs as particles near $220 \mu\text{m}$ diameter. Similar peaks have been reported in previous works (1, 11) on the basis of interpolation between data obtained with different methods, which had cast doubt as to whether the peak was real or an artifact introduced by the interpolation. The consistent measurement technique used in this study dismisses that concern and verifies the existence of a strong peak in the mass distribution. The total mass accreted by the Earth per year across the size range sampled here is $(40 \pm 20) \times 10^6 \text{ kg year}^{-1}$.

potentially larger error could exist if the velocity exponent in the Christiansen formula (Eq. 1) (21) is incorrect. The stated value of 0.667 is based on laboratory impact experiments of centimeter, millimeter, and micrometer projectiles striking thick aluminum alloy targets at speeds up to 18 km s^{-1} (although most of the data were obtained at velocities below 8 km s^{-1}), demonstrating that crater volume under those conditions is nearly proportional to the projectile kinetic energy (20, 21). Work by McDonnell and his colleagues (22) that makes use of submicrometer projectiles penetrating thin films at speeds up to 16 km s^{-1} suggests a velocity exponent of 0.806. We chose to base our calculations on the Christiansen formula because it more closely addresses our projectile size range and target properties. If another velocity exponent is shown to be more appropriate for the LDEF craters, then the functional fit to the crater size distribution (Fig. 1) can be used to adjust particle masses accordingly.

The cumulative mass distribution of meteoroids (Fig. 3) that we found with the Christiansen formula is similar in shape to, but significantly higher than, the model of Grün *et al.* (1), which relies on Apollo-era spacecraft measurements for masses below $5 \times 10^{-7} \text{ g}$ and the uncertain radar meteor data for masses near and above 10^{-5} g . The slope of the lower end of the current mass

function, and the dramatic change in that slope near $200 \mu\text{m}$ diameter, is consistent with predictions for a population of collision fragments (1, 29) spiralling sunward under Poynting-Robertson orbital decay, with the larger particles being removed by collisions on a time scale smaller than their transport time from initial orbit radii of 2 to 3 AU (1). This suggests a significant asteroidal contribution to the zodiacal dust complex.

There is a strong peak in the mass flux per log mass interval (Fig. 4) at $1.5 \times 10^{-5} \text{ g}$, which corresponds to particles $220 \mu\text{m}$ in diameter with density 2.5 g cm^{-3} and is within the large uncertainty of the previous estimates (1, 11). This peak also represents the particles carrying most of the kinetic energy flux. This study's consistent measurement scheme lays to rest previous concerns that the mass peak is an artifact introduced by interpolation of data acquired by different techniques across the mass range of interest.

Integration of the mass distribution (Fig. 4) yields a total accretion rate of $(40 \pm 20) \times 10^6 \text{ kg year}^{-1}$. The error was estimated from uncertainties in the meteoroid velocity and in the velocity exponent of the penetration depth formula. This result is two to three times higher than the small particle accretion rates of 15×10^6 and $16 \times 10^6 \text{ kg year}^{-1}$ estimated by Grün *et al.* (1) and Hughes (11), respectively. Our result is consistent with accretion-rate estimates derived from measurements of Ir in Antarctic ice (8) and deep-sea sediments (9) and of pelagic ^{53}Mn (7, 30); although, in each of these cases, the uncertainty is large. The LDEF flux is considerably higher than the estimated $3 \times 10^6 \text{ kg year}^{-1}$ of $>50\text{-}\mu\text{m}$ dust particles that survive atmospheric entry without vaporization (31), the $(0.4 \pm 0.3) \times 10^6 \text{ kg year}^{-1}$ estimated to survive entry without severe ^3He loss (10), and the $2 \times 10^6 \text{ kg year}^{-1}$ of meteoritic material that is delivered to the mesosphere and detected by lidar observations (32).

The best geochemical determination of the mass accretion rate for meteoroids of all sizes appears to be 49×10^6 to $56 \times 10^6 \text{ kg year}^{-1}$ from measurements of $^{187}\text{Os}/^{186}\text{Os}$ ratios in deep-sea sediments and Mn nodules (7). The factor of 3 to 4 difference between the Os measurements and the previous small meteoroid data (1, 11) was noted by Esser and Turekian (7) as evidence for significant mass contribution by meteoroids with masses larger than 10^6 g , a conclusion supported by the recent Spacewatch measurements of the near-Earth small asteroid population (13, 14). The LDEF small particle mass flux agrees well with the Os data. This is consistent with most of the extraterrestrial mass observed in the 10^5 -year time scale of the latter study, having been derived from small particles, and eliminates the requirement for a dom-

inant contribution from $>10^6$ -g objects. At the same time, it suggests that the significant mass flux from such bodies predicted on the basis of the Spacewatch results is not well represented in the geochemical data, possibly because it is distributed only locally.

In closing, we would like to note that the current extraterrestrial mass flux measurement could be improved by the use of detectors with larger surfaces or exposure times. Any experiments should, however, be carried out soon, as the projected increase in the flux of artificial orbital debris may seriously compromise the sensitivity of similar measurements in the future (33).

REFERENCES AND NOTES

1. E. Grün, H. A. Zook, H. Fechtig, R. H. Giese, *Icarus* **62**, 244 (1985).
2. G. J. Flynn and D. S. McKay, *J. Geophys. Res.* **95**, 14497 (1990).
3. W. H. Ip, *Nature* **345**, 511 (1990).
4. E. Anders, *ibid.* **342**, 255 (1989).
5. C. F. Chyba, P. J. Thomas, L. Brookshaw, C. Sagan, *Science* **249**, 366 (1990).
6. C. Chyba and C. Sagan, *Nature* **355**, 125 (1992).
7. B. K. Esser and K. K. Turekian, *Geochim. Cosmochim. Acta* **52**, 1383 (1988).
8. R. Ganapathy, *Science* **220**, 1158 (1983).
9. F. T. Kyte and J. T. Wasson, *ibid.* **232**, 1225 (1986).
10. M. Takayanagi and M. Ozima, *J. Geophys. Res.* **92**, E641 (1987); D. L. Anderson, *Science* **261**, 170 (1993).
11. D. W. Hughes, in *Cosmic Dust*, J. A. M. McDonnell, Ed. (Wiley, Chichester, United Kingdom, 1978), pp. 123–185.
12. G. W. Wetherill and E. M. Shoemaker, *Geol. Soc. Am. Spec. Pap.* **190**, 1 (1982).
13. D. L. Rabinowitz, *Astrophys. J.* **407**, 412 (1993); but see also D. L. Rabinowitz *et al.*, *Nature* **363**, 704 (1993) for discussion of possible origins of these objects.
14. Z. Ceplecha, *Astron. Astrophys.* **263**, 361 (1992).
15. R. J. Naumann, "The Near-Earth Meteoroid Environment," *NASA TN D-3717* (National Aeronautics and Space Administration, Washington, DC, 1966).
16. T. H. See *et al.*, in "LDEF—69 Months in Space," *NASA CP-3134*, A. S. Levine, Ed. (National Aeronautics and Space Administration, Washington, DC, 1991), pp. 477–486.
17. T. See, M. Allbrooks, D. Atkinson, C. Simon, M. Zolensky, *Meteoroid and Debris Impact Features Documented on the Long Duration Exposure Facility: A Preliminary Report* (Lyndon B. Johnson Space Center, Houston, TX, 1990).
18. M. R. Laurance and D. E. Brownlee, *Nature* **323**, 136 (1986).
19. J. A. M. McDonnell, S. P. Deshpande, D. H. Niblett, M. J. Neish, P. J. Newman, in *Proceedings of IAF/COSPAR World Congress*, W. Flury, Ed. (Pergamon, Oxford, in press).
20. B. G. Cour-Palais, *Int. J. Impact Eng.* **5**, 221 (1987).
21. E. L. Christiansen, *AIAA Pap.* #92-1462 (1992).
22. J. A. M. McDonnell and K. Sullivan, in *Proceedings of Workshop on Hypervelocity Impacts in Space*, J. A. M. McDonnell, Ed. (Unit for Space Sciences, University of Kent, Canterbury, United Kingdom, 1992), pp. 39–47.
23. F. Hörz *et al.*, in (16), pp. 487–501.
24. S. G. Love, D. J. Joswiak, D. E. Brownlee, in *Lunar Planet. Sci.* **XXIV**, 901 (1993).
25. J. E. Erickson, *J. Geophys. Res.* **73**, 3721 (1968).
26. D. J. Kessler, *AIAA J.* **7**, 2337 (1969).
27. H. A. Zook, in (16), pp. 569–579.
28. S. G. Love, University of Washington, thesis (1993).
29. J. S. Dohnanyi, in (11), pp. 527–605.
30. M. Imamura, T. Inoue, K. Nishiizumi, S. Tanaka,

paper OG 12-21 presented at the 16th International Cosmic Ray Conference, Kyoto, Japan, 1979.

31. M. Maurette, C. Jehanno, E. Robin, C. Hammer, *Nature* **328**, 699 (1987).
32. T. J. Kane and C. S. Gardner, *Science* **259**, 1297 (1993).
33. D. J. Kessler and B. G. Cour-Palais, *J. Geophys. Res.* **83**, 2637 (1978).
34. We thank W. M. Berrios and W. H. Kinard for providing access to the unique surfaces used in this experiment and D. H. Humes for advice and for preparation and handling of the panels. We

thank the LDEF Meteoroid and Debris Special Investigation Group for obtaining and archiving the crater images on panels H13, H19, and H25, especially T. H. See for extracting and transmitting the appropriate data. We also thank F. Hörz and H. A. Zook for useful advice and discussions, N. L. King for carrying out the small crater scan, and C. F. Chyba and an unidentified referee for valuable comments and suggestions on this paper. This work was supported by the National Aeronautics and Space Administration.

19 April 1993; accepted 20 August 1993

Melting of (Mg,Fe)SiO₃-Perovskite to 625 Kilobars: Indication of a High Melting Temperature in the Lower Mantle

A. Zerr and R. Boehler

The melting curves of two compositions of (Mg,Fe)SiO₃-perovskite, the likely dominant mineral phase in the lower mantle, have been measured in a CO₂ laser-heated diamond cell with direct temperature measurements and in situ detection of melting. At 625 kilobars, the melting temperature is 5000 ± 200 kelvin, independent of composition. Extrapolation to the core-mantle boundary pressure of 1.35 megabar with three different melting relations yields melting temperatures between 7000 and 8500 kelvin. Thus, the temperature at the base of the lower mantle, accepted to lie between 2550 and 2750 kelvin, is only at about one-third of the melting temperature. The large difference between mantle temperature and corresponding melting temperature has several important implications; particularly the temperature sensitivity of the viscosity is reduced thus allowing large lateral temperature variations inferred from seismic tomographic velocity anomalies and systematics found in measured velocity-density functions. Extensive melting of the lower mantle can be ruled out throughout the history of the Earth.

The interpretation and understanding of geochemical differentiation of the Earth, geodynamics, rheology, and, more recently, seismic tomography data hinge upon the melting temperatures of the lower mantle constituents: For example, (i) differentiation strongly depends on the degree of partial melting that occurred early in Earth's history; (ii) viscosity and anelasticity scale with the ratio of actual temperature over melting temperature, T/T_m ; and (iii) the melting temperature limits lateral temperature variations and the temperature contrast between the bottom of the mantle and the core. (Mg,Fe)SiO₃-perovskite is most likely the dominant phase in the lower mantle [up to ~20% magnesio-wüstite [(Mg,Fe)O] is also likely present]. Because perovskite melts closely to the eutectic in the MgO-SiO₂ system and the iron content of the mantle is only ~10%, the melting temperature of Mg-Fe-Si-perovskite represents a lower bound for the melting temperature of the lower mantle.

Earlier estimates of the melting curve of (Mg,Fe)SiO₃-perovskite show extreme variations, and melting temperatures pre-

dicted for pressures equivalent to those at the bottom of the mantle range from less than 2500 to 8000 K. Earlier experimental studies of melting of perovskite in the diamond cell have large uncertainties and are in strong contradiction to each other in both melting temperature and slope of the melting curve (1). Thermodynamic estimates rely on poorly known physical data obtained at low pressure and require a melting relation for extrapolation to mantle pressures (2). Molecular dynamics calculations do not provide meaningful constraints on the melting curve (3). More accurate multianvil data do not extend to pressures greater than 250 kbar (4) and yield only a weak constraint on the melting slope of perovskite above the majorite-perovskite-liquid triple point at about 220 kbar.

To reduce these uncertainties, we investigated the melting of Fe-Mg perovskite using a recently developed diamond-cell technique (5) in which thin section samples are embedded in an argon pressure medium and heated with a high-power CO₂ laser. This method circumvents the experimental problems of earlier laser-heating experiments, which caused large systematic errors; particularly, it avoids large temperature gradients and allows direct temperature

Max-Planck-Institut für Chemie, Postfach 3060, 55020 Mainz, Germany.